

Experimental study on the settling motion of coral grains in still water

Jie Chen^{1,2,3}, Zhen Yao¹, Fei He^{4,†}, Changbo Jiang^{1,2,3}, Chao Jiang¹, Zhiyuan Wu^{1,2,3}, Bin Deng^{1,2,3}, Yuannan Long^{1,2,3} and Cheng Bian¹

¹School of Hydraulic and Environmental Engineering, Changsha University of Science & Technology, Changsha 410114, PR China

²Key Laboratory of Dongting Lake Aquatic Eco-Environmental Control and Restoration of Hunan Province, Changsha 410114, PR China

³Key Laboratory of Water-Sediment Sciences and Water Disaster Prevention of Hunan Province, Changsha 410114, PR China

⁴School of Engineering, The University of Western Australia, 35 Stirling Highway, Crawley, WA 6009, Australia

(Received 18 April 2023; revised 4 May 2024; accepted 6 May 2024)

Understanding settling motion of coral grains is important in terms of protection of coral reef systems and resotation of the associated ecosystems. In this paper, a series of laboratory experiments was conducted to investigate the settling motion, using optical microscopy to measure shape parameters of coral grains and the particle-filtering-based object tracking to reconstruct the three-dimensional trajectory. Three characteristic descent regimes, namely, tumbling, chaotic and fluttering, are classified based on the three-dimensional trajectory, the spiral radius variation and the velocity spectrum. It is demonstrated that if one randomly picks up one coral grain, then the probabilities of occurrence of the three regimes are approximately 26 %, 42 % and 32 %, respectively. We have shown that first, the dimensionless settling velocity generally increases with the non-dimensional diameter and Corey shape factor and second, the drag coefficient generally decreases with the Reynolds number and Corey shape factor. Based on this, the applicability of existing models on predicting settling velocity and drag coefficient for coral grains is demonstrated further. Finally, we have proposed extended models for predicting the settling velocity. This study contributes to better understanding of settling motion and improves our predictive capacity of settling velocity for coral grains with complex geometry.

Key words: sediment transport

† Email address for correspondence: fei.he@research.uwa.edu.au

1. Introduction

Coral reef sediments have important implications for coral reef ecosystems. These sediments can provide the community (including reefs, fleshy algae and fish) with necessary carbonate and nutrients (Dong *et al.* 2023). However, with increased human activity, coral reef sediments are now even being considered as threats to the coral reef systems. Intense hydrodynamic disturbances – e.g. typhoons (Pratchett 2005), blast fishing and illegal poaching of tridacna (Scales, Balmford & Manica 2007) – can cause suspension of sediments (Jones *et al.* 2016; Rogers & Ramos-Scharrón 2022). These suspended sediments can settle directly on corals and other reef organisms, which will smother and abrade corals (Jones *et al.* 2016; Rogers & Ramos-Scharrón 2022). The suspended sediments can also reduce the coral photosynthesis by blocking light. The velocity of settling has been shown to influence the attachment and survival rates of coral larvae (Babcock & Smith 2002; Rogers & Ramos-Scharrón 2022). Understanding of settling motion and having predictive capacity for the settling velocity are critical in terms of helping to protect coral reef systems from those threats and restore the ecosystems effectively.

The settling motion has been explored in detail for a circular disk and a sphere with uniform shape but not for coral grains. For a circular disk, three regimes of settling trajectory were classified in Field *et al.* (1997), namely, fluttering, chaotic and tumbling. It has been demonstrated that the settling trajectory is highly dependent on the object geometry (Maiklem 1968). For a sphere, more fruitful regimes were observed (Raaghav, Poelma & Breugem 2022). In reality, the presence of biological structure of coral grains makes their geometry more complicated than the disk and sphere (Wang *et al.* 2020), which increases the complexity of settling motion (de Kruijf *et al.* 2021). Understanding the settling motion of coral grains is one of motivations of this study.

In the settling motion, when the effective force (gravity minus buoyancy) is equal to the drag force on the particle in the vertical direction (over the depth), the particle will fall with an equilibrium settling velocity ω . Different empirical models have been proposed for predicting the settling velocity for particles from different sources. For natural quartz, the model in Dietrich (1982) established the relationship of dimensionless velocity W^* with the non-dimensional particle diameter D^* (W^* and D^* are parameters non-dimensionalised by Reynolds number (Re) and drag coefficient). This relationship was then extended to carbonate grains in Li *et al.* (2020). This is different from the semi-empirical model proposed in Riazi *et al.* (2020) for carbonate sediments, in which the settling velocity is a function of S (the specific gravity of the particle), C_D (the drag coefficient), S_f (the Corey shape factor) and D_n (the nominal diameter). In comparison to these models, the model in Alcerreca, Silva & Mendoza (2013) simply established the relationship between Re and D^* (ω is embedded in Re).

There is also a range of models that can be used to estimate the drag coefficient C_D . First, the drag coefficient of a coral grain can be estimated through direct measurements of settling velocity, densities of coral grain and fluid, and the geometry of the grain. The drag coefficient can also be evaluated through the empirical model of Riazi *et al.* (2020), which links C_D to the nominal diameter and the kinematic viscosity of fluid. Finally, the drag coefficient can be predicted by the model of Wang *et al.* (2018), in which C_D is a function of Reynolds number and the Corey shape factor.

Although different models of settling velocity and drag coefficient have been developed in literature, grain shape parameters in these models still rely on some kind of approximation of spherical or tri-axial geometries. These approximated parameters sometimes are not that representative to the real geometry of coral grains. Since both

settling velocity and drag coefficient are highly dependent on the grain geometry (Maiklem 1968), applying these models to real systems can be problematic if the targeted grains are very different from the unknown particles used in the validation of the empirical models. This highlights the importance of using coral grains with fully categorised, quantified geometry to validate existing empirical models. In such a way, the applicable range of validated/modified models is well defined.

There is a range of approaches used to classify coral reef grains. For simplicity of classification, the coral grains were normally simplified into an ellipsoid (Wadell 1932; Krumbein 1941; Oakey *et al.* 2005). The long, medium and short axes of the ellipsoid (D_l , D_m and D_s) were found to be important dimensions in the classification. Based on the dimensionless variables D_m/D_l and D_s/D_m , coral grains were classified into four sub-populations, namely, discoid, blade, rod and spheroid (Zingg 1935). In contrast, based on a combined parameter set (D_m/D_l , D_s/D_l and $(D_l - D_m)/(D_l - D_s)$), the sediments can be categorised into four types: platy, bladed, elongated and compact (Sneed & Folk 1958). In comparison to these two classification methods based on the simplification of ellipsoid, there is another approach proposed in Wang *et al.* (2020). This approach was established based on both first- and second-order shape descriptors.

In the light of existing work, this paper aims to investigate the settling motion of 222 coral grains from the South China Sea, with three specific objectives: (1) categorise these coral grains; (2) classify the settling trajectory of coral grains; (3) validate and extend existing models for predicting settling velocity and drag coefficient.

2. Methodology

2.1. Geometric parameters

There are three orders of the scale for describing the shapes of irregular particles (figure 1): form, roughness and surface texture (Griffiths 1967; Barrett 1980). However, limited by the availability of measuring equipment, most studies on shape quantification have focused on the first and second orders of scale. In the first order of scale, form is the fundamental descriptor of the three-dimensional spatial distribution of a particle in space. As shown in figure 2, the lengths of three axes (i.e. long axis D_l , intermediate axis D_m , and short axis D_s) of the ellipsoid can characterise the three-dimensional spatial distribution of the particle (Barrett 1980; Oakey *et al.* 2005; Blott & Pye 2008; Heilbronner & Barrett 2013). Based on these dimensions, several dimensionless parameters are used to describe the form of the particles, such as the flatness D_s/D_m (Blott & Pye 2008), elongation D_m/D_l (Lüttig 1956), and equancy D_s/D_l (Illenberger 1991). Meanwhile, Wadell (1932, 1933) and Corey *et al.* (1949) defined the nominal diameter and the Corey shape factor, respectively, for the non-spherical grains as

$$D_n = \sqrt[3]{D_l D_m D_s}, \quad (2.1)$$

$$S_f = \frac{D_s}{\sqrt{D_l D_m}}. \quad (2.2)$$

In the second order of scale, roundness characterises the smoothness of the particles. Establishing the shape parameters at the roundness scale is usually achieved by quantifying the difference of the grain shape from the spherical shape (see figure 3) with the sphericity ϕ , a ratio between surface area $A_{eq, sph}$ of a sphere and that of the particle, A_p (the sphere has the same volume as the particle). However, the shape of coral sand particles is complex at the roundness scale (figure 1) due to the deposition processes in coral islands and

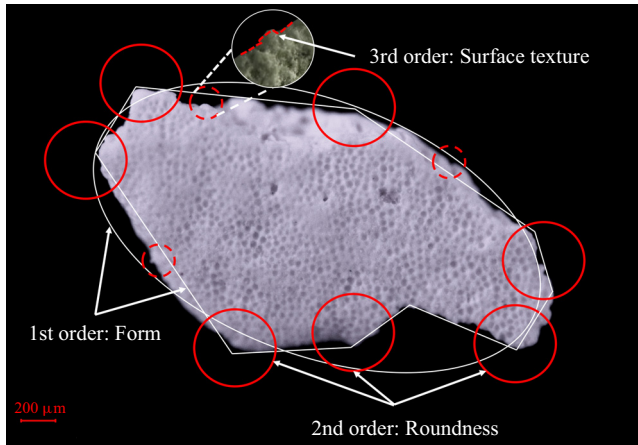


Figure 1. Shape descriptors of three orders for a coral grain.

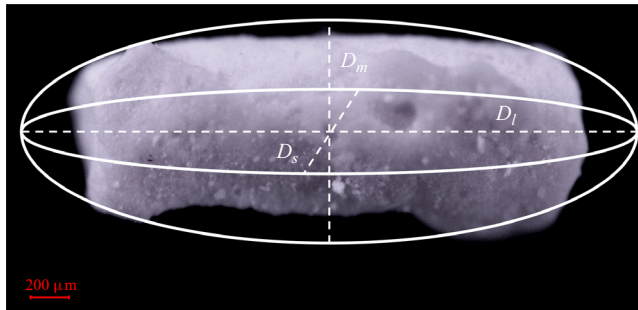


Figure 2. Tri-axial orthogonal system of the ellipsoid simplification of a real coral grain.

the presence of skeletal structures (Slootman *et al.* 2023). These parameters may not be sufficient to describe the geometry of coral particles. To address this, a new shape parameter ψ was proposed in Wang *et al.* (2018) for describing the highly irregular grains, which is defined as

$$\psi = \frac{\phi}{X}, \quad \phi = \frac{A_{eq, sph}}{A_p}, \quad X = \frac{P_{p, max}}{P_{eq}}, \quad (2.3a-c)$$

where ϕ is sphericity, $A_{eq, sph} = \pi(D_{eq, sph})^2$ is the surface area of the volume-equivalent sphere, $D_{eq, sph} = ((6/\pi)V_p)^{1/3}$ is the diameter of the volume-equivalent sphere, V_p is the particle volume, A_p is the surface area (which is calculated as $A_p \approx A_{ell} = \pi[(D_l D_m)^\kappa + (D_l D_s)^\kappa + (D_m D_s)^\kappa / 3]^{1/\kappa}$, with $\kappa = 1.6075$), A_{ell} is the surface area of the irregular particles under the tri-axial orthogonal system of the ellipsoid (figure 2), $P_{p, max}$ is the perimeter of the maximum projection area of the particle, and P_{eq} is the perimeter of a circle with the same maximum projection area as the particle.

The original classification method based on the first-order shape descriptors (figure 4) was unable to describe the particular shape of the coral sand grains (see figure 1) due to the complexity of the particle shape. Wang *et al.* (2019) summarised a series of the first-order and second-order shape descriptors from the studies of Mora & Kwan (2000), Kwan, Mora & Chan (1999) and Hentschel & Page (2003) (see table 1). Wang *et al.* (2019) then classified coral grains into dendrites, rods, flakes and blocks based on both first-

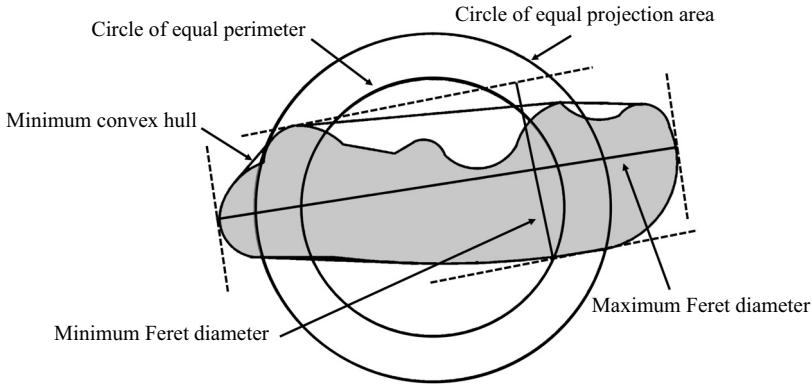


Figure 3. Diagram of shape descriptors reported in Wang *et al.* (2019).

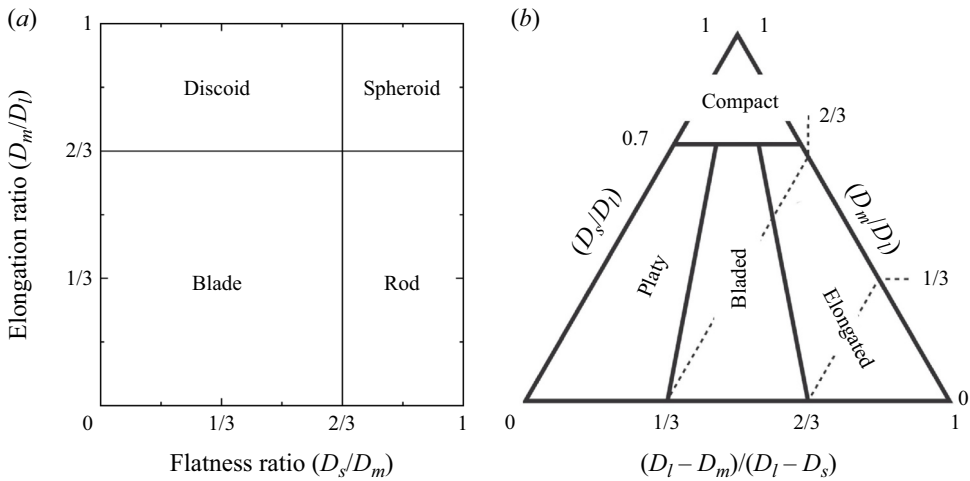


Figure 4. Irregular particle classification based on the first-order shape descriptors: (a) classification diagram from Zingg (1935), and (b) equant–oblate–prolate ternary classification diagram by Sneed & Folk (1958).

and second-order shape descriptors (tables 2 and 3). These descriptors based on three dimensions were determined with multi-photographs taken from different angles of view.

2.2. Predictive models of drag coefficient and settling velocity

2.2.1. Models for estimating C_D

(i) Model I_D (direct measurement)

When the effective weight is equal to the drag force of particle in the vertical direction, the particle falls with terminal settling velocity. At this stage, the momentum balance in the vertical direction (over depth) can be expressed as

$$(\rho_s - \rho)gV = \frac{1}{2}\rho C_D A_P \omega^2, \quad (2.4)$$

where ρ_s and ρ are the densities of coral grain and fluid, respectively, g is the gravitational acceleration, V is the volume of the coral grain, C_D is the drag coefficient, A_P is the maximum projected area of the particle, and ω is the particle

Parameter	Description	2-D definition	3-D definition
Area	A	Area of image	Mean A value of a series of images
Perimeter	C_i	Perimeter of image	Mean C_i value of a series of images
Convex area	C_A	Area of minimum convex hull	Mean C_A value of a series of images
Convex perimeter	C_P	Perimeter of minimum convex hull	Mean C_P value of a series of images
Feret diameter	F_a	Distance between two parallel tangents of the particle at an arbitrary angle	—
Length	L	Maximum Feret diameter	Maximum length in a series of images
Width	W	Width	Maximum width in a series of images
Thickness	T	—	Minimum width in a series of images
Diameter of a circle of equal projection area	D_A	Diameter of a circle that has the same area as the projection area of the particle	Mean D_A value of a series of images
Diameter of a circle of equal perimeter	D_P	Diameter of a circle that has the same perimeter as the image	Mean D_P value of a series of images

Table 1. Two-dimensional (2-D) and three-dimensional (3-D) first-order shape descriptors.

Parameter	Description	Formula
Superficial area	S_A	Area of the particle in the image
Superficial area of convex hull	S_{CA}	Perimeter of the particle in the image
Volume	V_{ch}	Area of minimum convex hull
Convexity ratio	S_0	$S_0 = A/C_A$
Roundness	R_0	$R_0 = 4A/(\pi L^2)$
Width-to-thickness ratio	W/T	—
Elongation ratio	L/W	—
Relative sphericity	S_P	$S_P = D_A/D_P$
Convex ratio	C_0	$C_0 = C_P/P$

Table 2. Particle shape parameters in Wang *et al.* (2019).

Parameter	Rod	Flake	Dendrite	Block
Elongation ratio	> 1.8	—	—	Others
Width-to-thickness ratio	< 1.8	> 1.8	> 1.2	
Relative sphericity	—	—	< 0.76	
Roundness	> 0.85	> 0.85	< 0.85	

Table 3. Classification criteria for calcium sand with various shapes in Wang *et al.* (2019).

settling velocity. Equation (2.4) can be rewritten in the form

$$C_D = 2 \frac{(S - 1)g}{\omega^2} \frac{V}{A_P}, \quad (2.5)$$

where $S = \rho_s/\rho$ is the specific gravity of the particle. The drag coefficient can be determined by measuring all the quantities on the right-hand side of (2.5).

(ii) **Model II_D (Riazi *et al.* 2020)**

Based on the data of Smith & Cheung (2002), Riazi *et al.* (2020) used a genetic algorithm (Riazi & Türker 2018) to obtain an expression for C_D of coral grains:

$$C_D = \left(\frac{9.50 \times \nu}{D_n^{1.5} \times g^{0.5}} + 0.76 \right)^{2.92} + \left(\frac{20.47 \times \nu}{D_n^{1.5} \times g^{0.5}} + 1.02 \right)^{-48.15}, \quad (2.6)$$

where ν is the kinematic viscosity of the fluid.

(iii) **Model III_D (Wang *et al.* 2018)**

Wang *et al.* (2018) obtained the relationship between drag coefficient and Reynolds number based on experimental data of 521 calcareous sand particles, which is expressed by

$$\left. \begin{aligned} C_D &= 0.945 \frac{C_{D, sph}}{\psi^{f(Re)}} Re^{-0.01}, \\ C_{D, sph} &= \frac{24}{Re} \left(1 + 0.15 Re^{0.687} \right) + 0.42 \left/ \left(1 + \frac{42500}{Re^{1.16}} \right) \right., \\ f(Re) &= 0.641 Re^{0.153}, \\ Re &= \frac{\rho \omega D_n}{\mu}. \end{aligned} \right\} \quad (2.7)$$

2.2.2. Models for predicting setting velocity

(i) **Model I_V (Riazi *et al.* 2020)**

Using an approximation of ellipsoids to natural particles, Riazi *et al.* (2020) found that the ratio of the volume V to the projected area A_P is a function of S_f and D_n , with the relationship

$$\frac{V}{A_P} = \alpha \frac{2}{3} (S_f)^{(2/3)} D_n, \quad (2.8)$$

where $\alpha = 0.55$ based on their experimental data. The derivation of (2.8) was based on extensive observations that natural particles will adjust themselves into a state where the maximum projected area ($A_p = \pi D_l D_m / 4$) is normal to the settling direction, regardless of the orientation of the particle being realised into fluid (Dietrich 1982; Alldredge & Gotschalk 1988; Khatmullina & Isachenko 2017; Riazi & Türker 2019). Equation (2.8) was validated here by measuring variables on both sides of this equation, which gives measured values of α . The root mean square error (RMSE) between the measured values of α and 0.55 determined by Riazi *et al.* (2020) is 32.5 % for our 222 coral grains, which supports the applicability of this equation to the present study.

Equation (2.4) can be rewritten as

$$\omega^2 = 2 \frac{(S-1)g}{C_D} \frac{V}{A_P}. \quad (2.9)$$

Combining (2.8) with (2.9) gives

$$\omega^2 = \alpha \frac{4}{3} \frac{(S-1)g}{C_D} S_f^{2/3} D_n. \quad (2.10)$$

Note that C_D is unknown in (2.10). In practice, this model needs to be combined with the drag model II_D to provide a closed-form solution for both the velocity and the drag coefficient.

(ii) **Model II_V (Dietrich 1982)**

Many researchers (Rouse *et al.* 1938; Schulz, Wilde & Albertson 1954; Dietrich 1982) have described the settling velocity in a dimensionless form of W^* as

$$W^* = \left[\left(\frac{4}{3} \right) \frac{Re}{C_{D, sph}} \right]^{-1/3} = \omega [vg(S-1)]^{-1/3}. \quad (2.11)$$

By analogy, the particle diameter was also expressed as

$$D^* = \left[\frac{3}{4} (Re)^2 C_{D, sph} \right]^{1/3} = D \left[\left(\frac{1}{v} \right)^2 g(S-1) \right]^{1/3}. \quad (2.12)$$

Dietrich (1982) collected a large amount of experimental data of natural silicate particles and proposed a model of settling velocity based on particle shape characteristics (particle size D^* , particle shape S_f , particle roughness P):

$$\left. \begin{aligned} W^* &= R_3 10^{R_1 + R_2}, \\ R_1 &= -3.76715 + 1.92944 \log D^* - 0.09815 (\log D^*)^2 \\ &\quad - 0.00575 (\log D^*)^3 + 0.00056 (\log D^*)^4, \\ R_2 &= \log \left(1 - \frac{1 - S_f}{0.85} \right) - (1 - S_f)^{2.3} \tanh(\log D^* - 4.6) \\ &\quad + 0.3(0.5 - S_f)(1 - S_f)^2 (\log D^* - 4.6), \\ R_3 &= \left[0.65 - \frac{S_f}{2.83} \tanh(\log D^* - 4.6) \right]^{1 + (3.5 - P)} - 4.6. \end{aligned} \right\} \quad (2.13)$$

(iii) **Model III_V (Li *et al.* 2020)**

Li *et al.* (2020) modified the model of Dietrich (1982) and extended it to 320 sets of platy shell fragments, with the simplified form

$$W^* = 10^{a \log(D^*) + b \log(S_f) + c}, \quad (2.14)$$

where $a = 0.416651$, $b = 0.5316$ and $c = 0.3891$.

(iv) **Model IV_V (Alcerreca *et al.* 2013)**

To have a quick prediction tool, Alcerreca *et al.* (2013) developed a model of settling velocity based on 1557 calcareous sand grains as

$$Re = \left(\sqrt{22 + 1.13D^{*2}} - 4.67 \right)^{3/2}. \quad (2.15)$$

Equation (2.15) can be rewritten in the form of settling velocity as

$$\omega = Re \frac{v}{D_n} = \frac{v}{D_n} \left(\sqrt{22 + 1.13D^{*2}} - 4.67 \right)^{3/2}. \quad (2.16)$$

2.2.3. *Performance metric*

In this paper, the RMSE is used as a metric for evaluating the performance of different models:

$$\text{RMSE}(\%) = \left(\frac{\sum (\text{Estimated} - \text{Measured})^2}{\sum (\text{Measured})^2} \right)^{0.5} \times 100. \quad (2.17)$$

A smaller RMSE value indicates better model performance.

2.3. *Experimental set-up*

A series of experiments was conducted to study the settling motion of the coral grains at the Hydraulic Engineering Laboratory, Changsha University of Science and Technology, China. A Plexiglas tank (0.3 m long, 0.3 m wide and 0.8 m deep) was designed for the test, and the tank was filled with water at temperature $24 \pm 3^\circ\text{C}$, density $\rho = 1000 \text{ kg m}^{-3}$ and dynamic viscosity $\mu = 1.247 \times 10^{-3} \text{ Pa s}$. The water depth in the tank was maintained at 0.80 m in the experiments. Since there are pores in the dry coral grains, bubbles will be generated from the particles when they settle down. To avoid the influence of bubbles on the settling motion, dry coral grains were immersed in the water for 24 h before testing. There was a minimum relaxation time of 5 min between each experiment, to ensure the water is truly still in the tank before the next run. The coral grain was cleaned from the bottom after each experiment such that it will not occupy the volume in the tank to increase the water depth.

Figure 5 shows the experimental set-up. The background water in the tank was illuminated using a continuous laser sheet, and the light source had wavelength 532 nm (Laserwave, G2000). Black curtains were placed around the tank to eliminate wall reflections of light. The settling motion of a coral grain in the water was recorded with two high-speed cameras (FASTCAM Mini UX100 and MEMRECAM HX-7S) in two orthogonal directions (see figure 5a). Both cameras were equipped with AF50 mmf/1.8DI camera lenses (Nikon, Japan) and had resolution 1024×1024 pixels. Raw images were recorded at 50 Hz, which was controlled by computer image capture software (Photron Motion Tools). The camera was calibrated by the MATLAB toolbox ‘camera calibrator’.

The volume of interest was a cuboid measuring $0.30 \text{ m} \times 0.30 \text{ m} \times 0.25 \text{ m}$ (see figure 5b). To reconstruct the settling process of the coral grains, the algorithm for particle filtering was implemented in MATLAB, for which the regionprops library was used. The positions of a coral grain in settling were tracked (in MATLAB) from images taken at every moment (figure 6). After the particle had undergone the initial acceleration phase (Heisinger, Newton & Kanso 2014), it entered the vertical force equilibrium phase (see

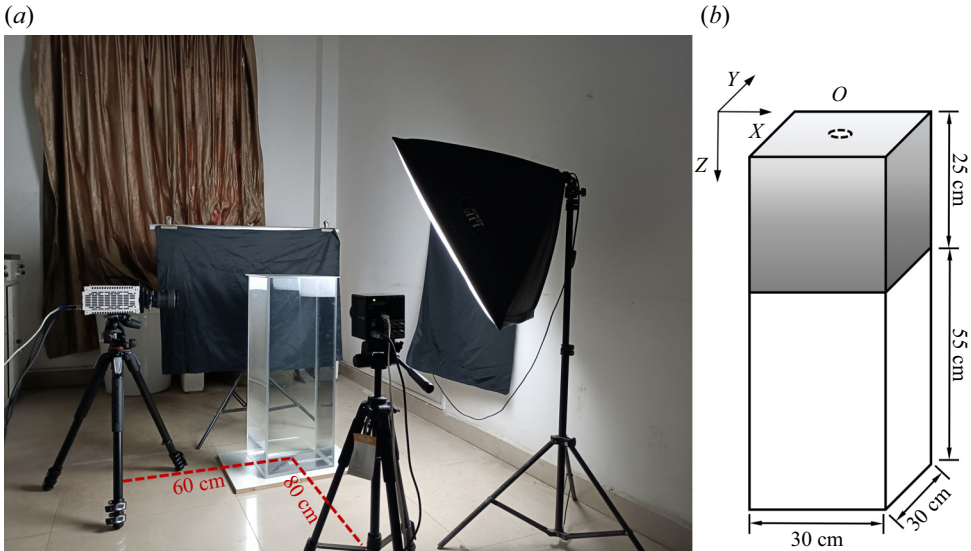


Figure 5. (a) Image of experimental set-up for monitoring the settling motion of coral grains by a charge-coupled device (CCD) camera (in the X and Y directions, respectively). (b) Sketch of the acrylic tank in (a). The volume ($30\text{ cm} \times 30\text{ cm} \times 25\text{ cm}$) monitored by the two cameras is shaded in grey. A coral sand particle was released from the point O without initial velocity.

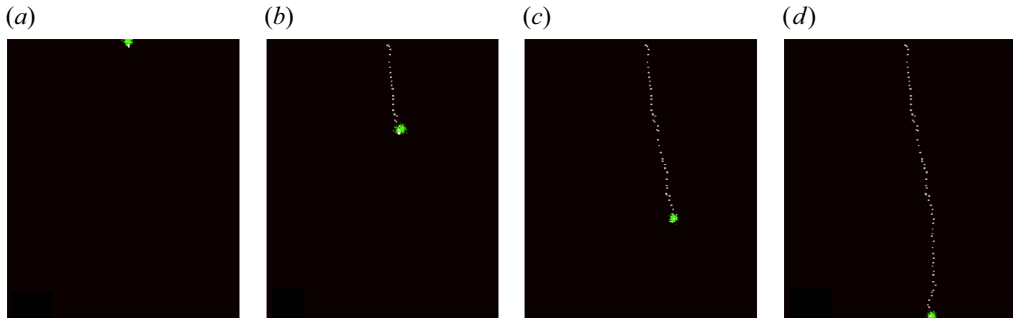


Figure 6. An example of the settling trajectory of a particle tracked by the particle filtering algorithm based on MATLAB. White dots in each image represent the historical particle positions, and each dot was processed from one image. The green dot in each image represents the particle position at the moment.

figure 7). Each particle was tested five times. The terminal settling velocity of the particle was calculated by averaging velocities of the five repeated runs. The relative error (2.18) for all the cases in the present work is less than 5 %, demonstrating the repeatability of experiments (see table 4):

$$Q_i = \frac{\sum_{j=1}^5 \left| \frac{\omega_j - \omega}{\omega} \right|}{5} \times 100\%. \quad (2.18)$$

The lengths of the long, middle and short axes (D_l , D_m and D_s , respectively) were measured by the following procedure. Specifically, following fluorescence microscopy (OLYMPUS BX43), the grain was first placed on the microscope stage, and a photograph

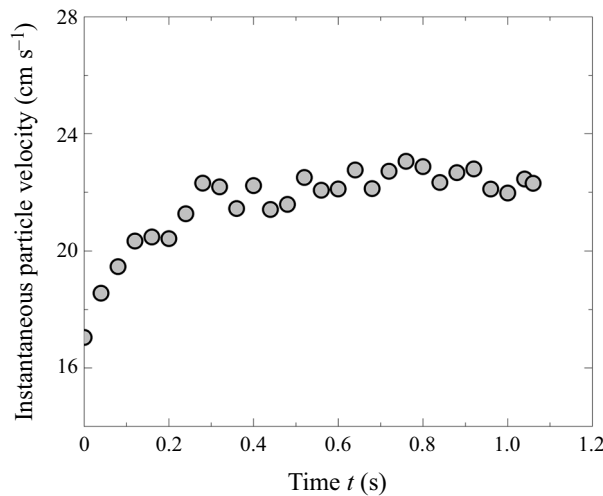


Figure 7. The temporal evolution of the particle velocity in the settling motion for a coral grain with $D_n = 2.63$ mm.

No.	ω_1 (cm s ⁻¹)	ω_2 (cm s ⁻¹)	ω_3 (cm s ⁻¹)	ω_4 (cm s ⁻¹)	ω_5 (cm s ⁻¹)	ω (cm s ⁻¹)	Relative error Q
1	16.383	15.851	15.822	16.839	16.057	16.190	2.08 %
2	21.441	21.758	21.617	20.872	21.258	21.389	1.21 %
3	15.118	15.937	14.871	15.296	15.342	15.312	1.71 %
4	19.378	18.823	18.750	19.6875	20.588	19.445	2.85 %
5	12.963	13.315	13.581	12.806	12.683	13.069	2.32 %
6	8.237	8.075	8.004	8.209	8.707	8.246	2.23 %
7	23.248	23.273	22.336	23.583	22.833	23.054	1.63 %
8	26.335	27.225	25.779	26.495	26.301	26.427	1.31 %
9	20.952	21.003	21.501	20.725	21.193	21.074	1.03 %
10	13.797	12.356	14.518	13.297	14.234	13.640	4.77 %

Table 4. Relative error of repeated tests.

was taken of it. After this, the grain was rotated about the axis along which the distance across the particle is visually longest. Then another photograph was taken of this newly positioned grain. Repeating this process produces multi-angle photographs. In each photograph, the length and width of the grain can be determined through two approaches in OpenCV (Zingg 1935; Wang *et al.* 2018) as illustrated in figure 8. Specifically, the length and width can be determined through the minimum outer rectangle measurement (figure 8a) or the best fitting ellipse measurement (figure 8b). The largest length among these photographs was defined as the long axis length D_l . Among widths in these photographs, the longest one was defined as the middle axis length D_m , whereas the shortest one was considered as the short axis length D_s .

A total of 222 experiments were conducted to investigate the settling motion of coral grains. The experimental particles conform to the coral and gastropod grains described in de Kruijf *et al.* (2021). Coral grains were sieved into 10 groups using 10 sieve shakers with sieve numbers ranging from 0.25 mm to 5 mm. To measure the density of coral grains, a set of coral grains with total mass 100 g was picked from one of groups. The volume of

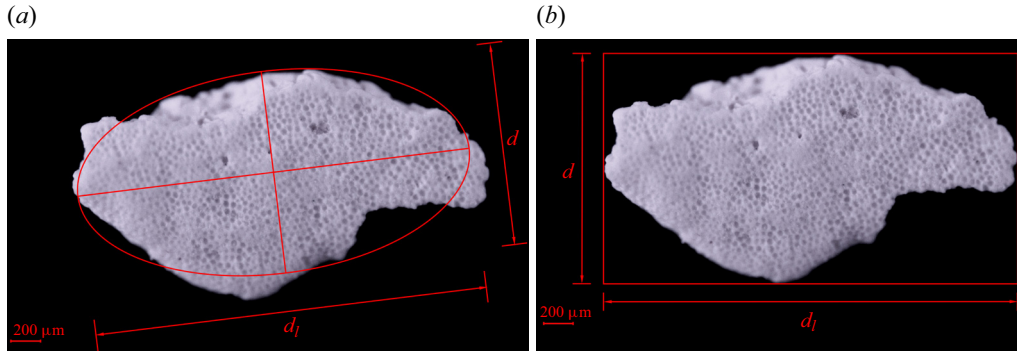


Figure 8. Determination of three ellipsoid axes based on image recognition. (a) Approach of the best-fit ellipse of ImageJ from Wang *et al.* (2018). (b) Approach of the minimum bounding rectangle from Chen *et al.* (2022).

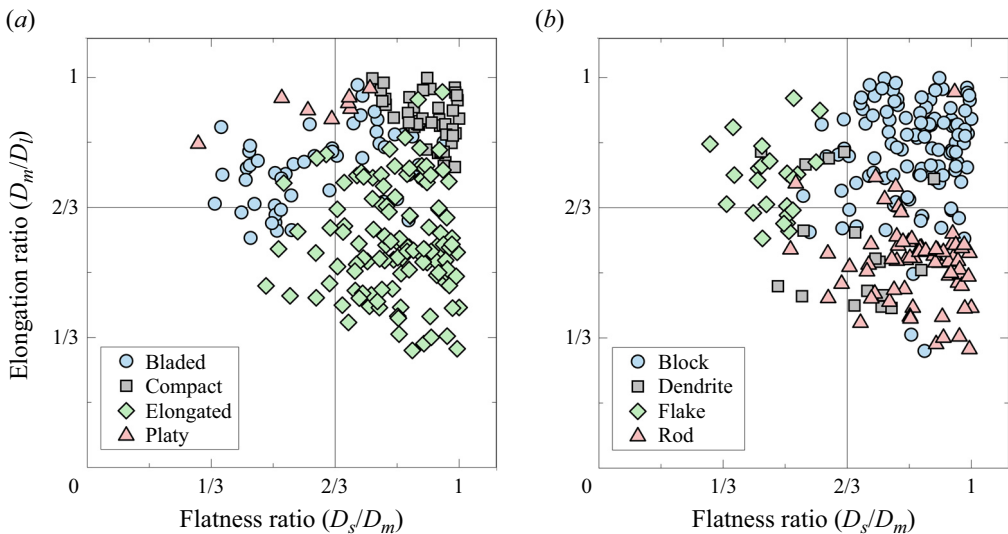


Figure 9. (a) Mapping coral grains classified by the method of Sneed & Folk (1958) into the parameter space defined by Zingg (1935). (b) Mapping coral grains classified by the method of Wang *et al.* (2019) into the parameter space defined by Zingg (1935).

this set of grains was measured through the drainage method. In such a way, the density for this set of grains was determined. Repeating this process for each group of sieved coral grains yielded individual densities. Averaging these 10 densities gives the real density (2700 kg m^{-3}) for these mixed coral grains.

In our experiments, the coral grains classified by Zingg (1935) and Wang *et al.* (2019) are both mapped out in the parameter space defined by Sneed & Folk (1958) in figure 9. Wide ranges of D_n (1.47–5.23 mm) and S_f (0.22–0.99) were examined (see figures 10 and 11), which covered the nominal diameter range of Hongbing, Sun & Cheng (2006) for the Nansha Islands. The distribution of the range of shape coefficients for different shapes of coral sand particles is shown in figure 11.

Note that all the symbols used in this paper are summarised in the Appendix.

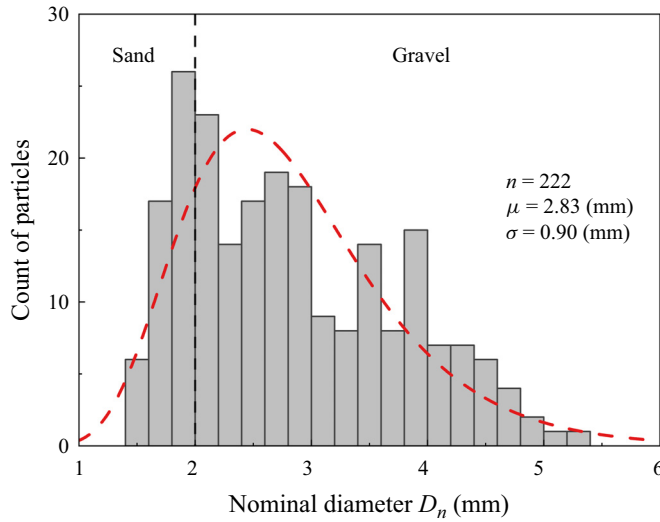


Figure 10. Distribution of nominal diameter D_n for a total of $n = 222$ grains. Here, μ is the mean, and σ is the standard deviation.

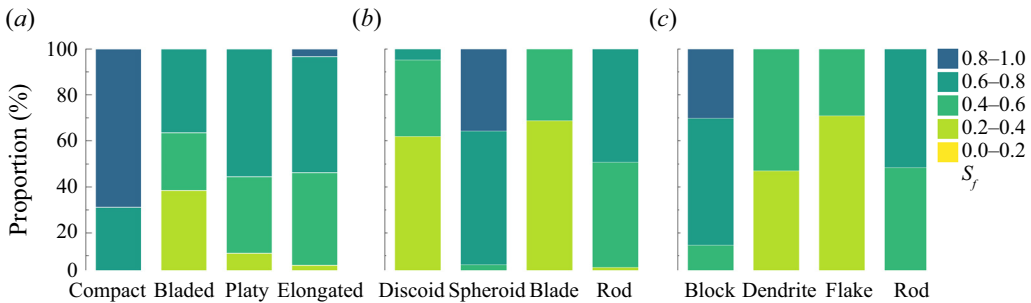


Figure 11. Proportion of each type of coral grain within each interval of shape factor S_f . A total of 222 coral grains were classified by the methods of (a) Sneed & Folk (1958), (b) Zingg (1935), and (c) Wang *et al.* (2019).

3. Results

3.1. Classification of descent regimes of coral grains

With laboratory experiments, three regimes of settling motion are classified for coral grains based on the reconstructed three-dimensional settling trajectory, the spiral radius r defined as

$$r = \sqrt{X^2 + Y^2}, \quad (3.1)$$

and the spectrum of settling velocity (see figure 12). The regime classification is based on the fully developed motion for which the settling velocity reaches an equilibrium state. The three regimes, namely, fluttering, tumbling and chaotic, are similar to those identified for spherical (Raaghav *et al.* 2022) and disk-like particles (Field *et al.* 1997).

The fluttering regime is characterised by a three-dimensional spiral trajectory about a vertical axis (see figure 12a). The projection of the trajectory in the x - y plane forms an elliptical path (figure 12a). This elliptical path is further demonstrated by figure 12(b), where the normalised spiral radius r/r_{max} first increases and then decreases with time, with values of r/r_{max} equal at two ends of t/t_{max} (figure 12b). The spiral forms oscillations

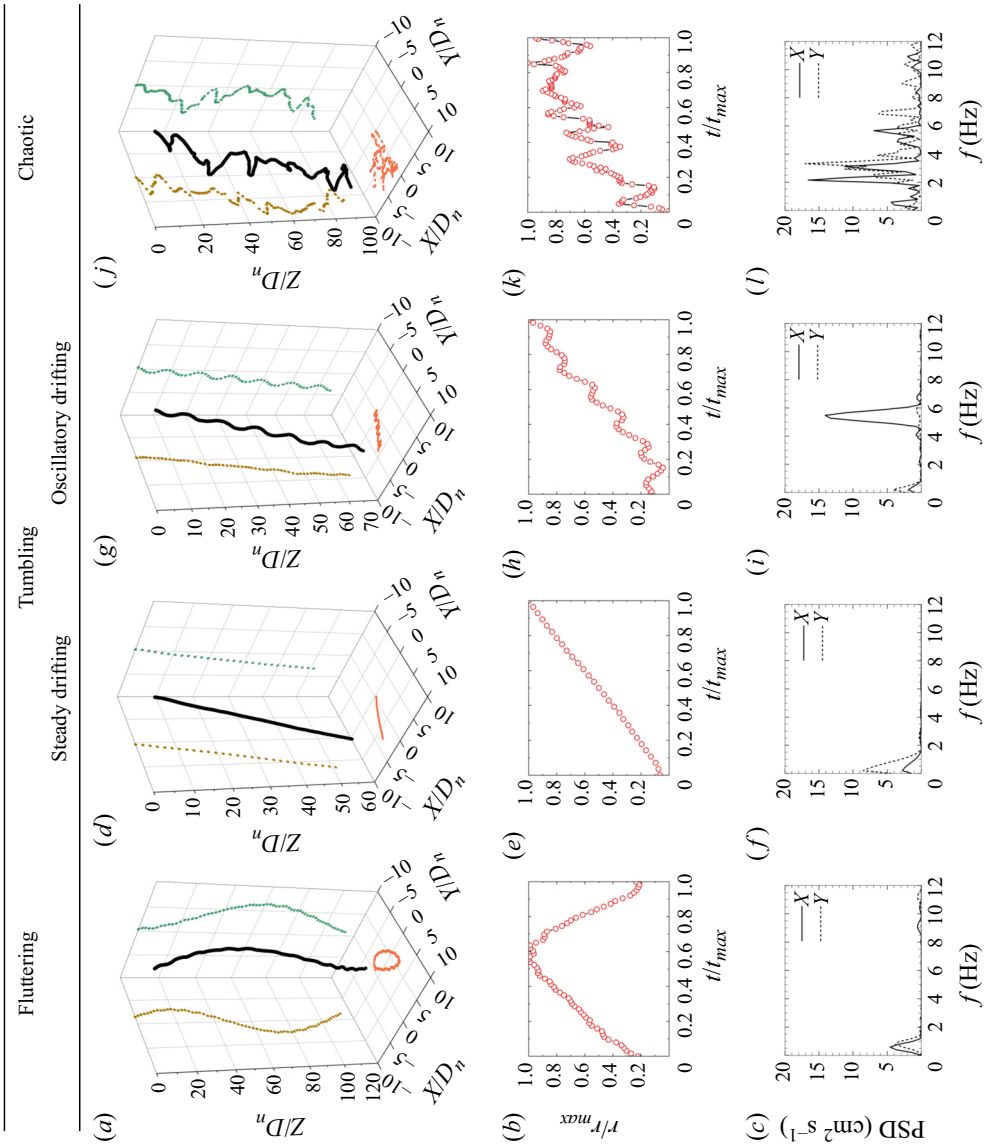


Figure 12. Regime classification of settling trajectory. *(a,d,g,i)* Reconstructed three-dimensional trajectory with the projections of trajectory in different planes, with $D^* = 49, 72, 90, 75$, $W^* = 6.5, 9.6, 7.2, 4.0$ and $S_f = 0.84, 0.74, 0.40, 0.22$. *(b,e,h,k)* Variation of normalised spiral radius with time. *(c,f,i,l)* Spectra of velocities in the x and y directions. Fluttering, tumbling and chaotic regimes are characterised by a spiral trajectory in *(a)*, sideways drifting in *(d,g)*, and a chaotic trajectory in *(i)*, respectively.

in both the x - z and y - z planes, with wavelength approximately $120D_n$ (figure 12a). The oscillations in these two planes are indicated by two dominant peaks ($f = 0.58, 0.78$ Hz) respectively in the spectra of velocities on the x and y axes (see figure 12c).

In the tumbling regime, a grain drifts sideways when settling downwards, as shown by the three-dimensional trajectory in figures 12(d,g). The projection of the trajectory in any plane displays a path extending in a particular direction (figures 12d,g). The tumbling regime has two sub-regimes, i.e. steady drifting regime and oscillatory drifting regime. The grain purely drifts in the steady drifting regime (figure 12d), in contrast to the oscillatory drifting regime where the drifting is accompanied by small-scale oscillations with wavelength $10D_n$ (figure 12g). Consistently, the spiral radius shows a linear variation with time in the steady drifting regime (figure 12e), whereas periodic fluctuations are superimposed on the increase of r/r_{max} in the oscillatory drifting regime (figure 12h). The drifting behaviour in the tumbling regime is indicated by dominant peaks at $f \approx 0$ Hz (figures 12f,i). For the oscillatory drifting regime, another dominant peak appears at $f = 5$ Hz in the x -velocity spectrum but not in the y -velocity spectrum (figure 12i). The oscillation occurs on only one axis (figure 12g), which distinguishes it from the fluttering regime where the spiral creates oscillations on both x and y axes (see figure 12a).

The chaotic regime is characterised by a random combination of drifting and spiral (figure 12j). The spiral radius fluctuates irregularly with time (figure 12k). The chaotic nature of this regime is indicated by multiple peaks spanning a broad range 1–10 Hz in the velocity spectra (figure 12l).

The settling regime depends on the geometry of coral grains. To demonstrate this, the coral grains are classified based on three existing approaches in figure 13.

First, coral grains can be classified into compact, bladed, platy and elongated by following Sneed & Folk (1958) (figures 13a,b). For bladed and elongated grains, the probabilities of occurrence of the fluttering, chaotic and tumbling regimes are close to each other (figure 13a). Distinctly, for the platy grains, only chaotic and tumbling regimes are observed, with occurrence probabilities 60 % and 40 %, respectively (figure 13a). The highest occurrence probability (39 %) of the fluttering regime appears for compact grains.

Second, for the classification method of Zingg (1935), the probabilities of occurrence of the fluttering, chaotic and tumbling regimes approach each other for the discoid and spheroid grains (figures 13c,d). For the blade grains, the occurrence probability of the chaotic regime is up to ~ 60 % (figure 13c). The rod grains have highest occurrence probabilities for both the fluttering and tumbling regimes (figure 13c).

Finally, when following the method of Wang *et al.* (2020), it is found that the occurrence probability of the chaotic regime is approximately 71 % for flake grains, with 21 % and 8 % for the fluttering and tumbling regimes, respectively (figures 13e,f). In contrast, the highest probability is 56 % for the fluttering regime of the dendrite grains. For the rod and block grains, the occurrence probabilities of tumbling regimes are significantly increased relative to the other two types of grains (figure 13e).

The averages of probabilities of occurrence of the tumbling, chaotic and fluttering regimes across the four different types of grains are approximately 26 %, 42 % and 32 %, respectively, regardless of the classification methods applied (see figures 13a,c,e). This suggests that if one randomly picks up one coral grain, then the probabilities of occurrence of the three regimes are approximately 26 %, 42 % and 32 %, respectively.

Whilst the dendrite grains have the highest occurrence probability (56 %) of the fluttering regime, the flake grains have the highest probability (71 %) of occurrence of the

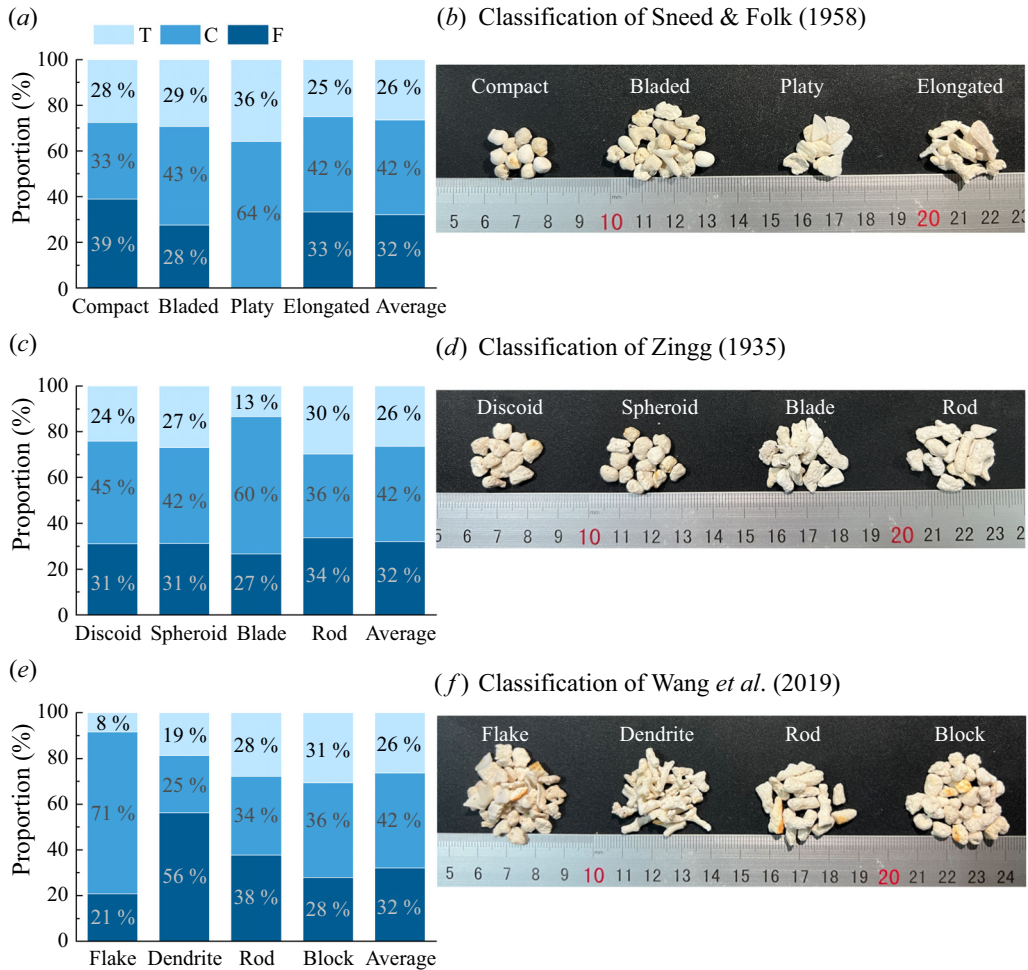


Figure 13. Probabilities of occurrence of fluttering (F), chaotic (C), and tumbling (T) regimes for different shapes of coral grains classified based on three previous approaches. The fifth column in (a,c,e) represents the average percentage of each regime across four different shapes of classified grains. The probability of occurrence of each regime differs between different types of grains, demonstrating the dependence of descent regimes on the geometry of grains.

chaotic regime. The tumbling regime occurs most likely for platy grains (36 %). Clearly, these are higher than the averaged probabilities (32 %, 42 %, 26 %) shown above. This means that classifying the grains based on existing methods to some extent can help to improve our predictive accuracy of descent regimes for a given coral grain.

3.2. Prediction of settling velocity and drag coefficient

In this subsection, the applicability of existing empirical models for predicting settling velocity W^* and drag coefficient C_D is demonstrated. Whilst the models of settling velocity are based mostly on dimensionless diameter D^* and the Corey shape factor S_f , the models of drag coefficient are based primarily on the Reynolds number Re and shape parameters. Therefore, to validate these models in predicting the settling velocity and the drag coefficient, we start by demonstrating the dependencies of W^* on D^* and S_f , and C_D

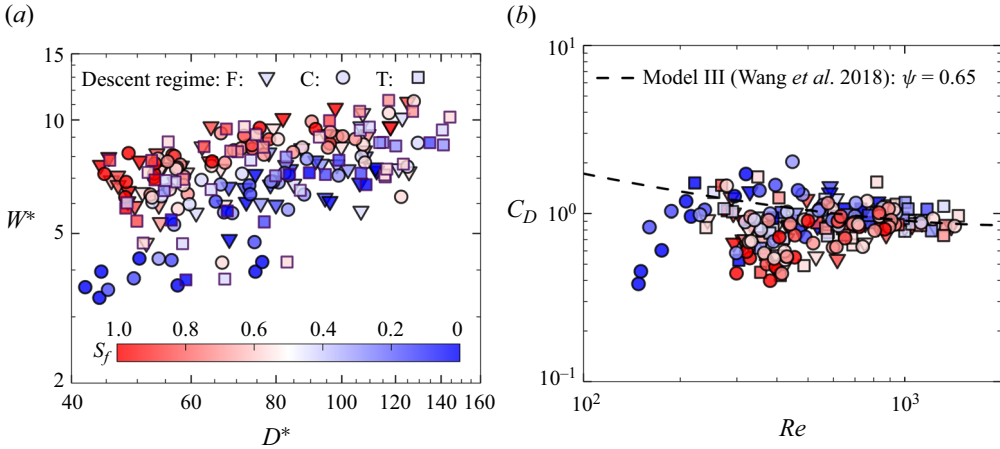


Figure 14. (a) The variation of settling velocity with the dimensionless diameter and shape factor. (b) The variation of drag coefficient with the particle Reynolds number and shape factor. The result from the model of Wang et al. (2018) is incorporated in (b) for comparison. In both (a,b), regimes are differentiated by different symbols. Whilst the dependence of settling velocity on W^* and S_f is demonstrated in (a), the relationship of drag coefficient with Re and S_f is confirmed in (b).

on Re and S_f , with experimental measurements in figure 14, which provides a physical basis for applying these models.

Figure 14(a) shows that the settling velocity generally increases with D^* and S_f . For the same D^* , for instance $D^* = 80$, with increasing S_f from 0 to 1, the settling velocity can even vary from 4 to 10 by a factor of 2. This suggests that the settling velocity increases as the shape of a particle increasingly approaches the sphere. This velocity becomes less sensitive to the particle shape with increasing D^* . The data points in the chaotic regime set the lower limit of W^* when $D^* < 80$ and $S_f \rightarrow 0$. This implies that a non-spherical coral grain in the chaotic regime generally has lower settling velocity relative to that in the other two regimes when $D^* < 80$.

In contrast, the drag coefficient generally decreases with Re and S_f (figure 14b). The measured data are in agreement with those predicted by model III_D of Wang et al. (2018). The decreasing trend of C_D with Re is consistent with previous work about flow past a stationary plate and sphere (e.g. Almedeij 2008; Duan, He & Duan 2015) in the range $Re \sim O(10^2-10^3)$. There are some data points deviating from this predicted curve, which are mostly from the chaotic regime and at two ends of S_f . This is expected since there are complex self-rotations superimposed on the vertical settling motion (observed in experiments) for these deviated data points, which may suppress the shear layer separation from the grain surface and hence reduce the form drag of the grain.

With the demonstrated dependencies of W^* and C_D above, we now can validate the existing models by presenting comparisons between the measurements and predictions of velocity and drag coefficient in figure 15. In the comparisons, we retain the velocity forms including W^* , ω and Re , as presented originally in these velocity models.

There is a large difference in the prediction accuracy among different velocity models. First, model I_V of Riazi et al. (2020) provides the best prediction of settling velocity ω with RMSE = 15.9% (figure 15a). In comparison to the other three types of grains, model I_V provides less good predictions of ω for the rod grains. While model I_V largely overpredicts the velocity, model II_V of Dietrich (1982) generally underpredicts W^* using

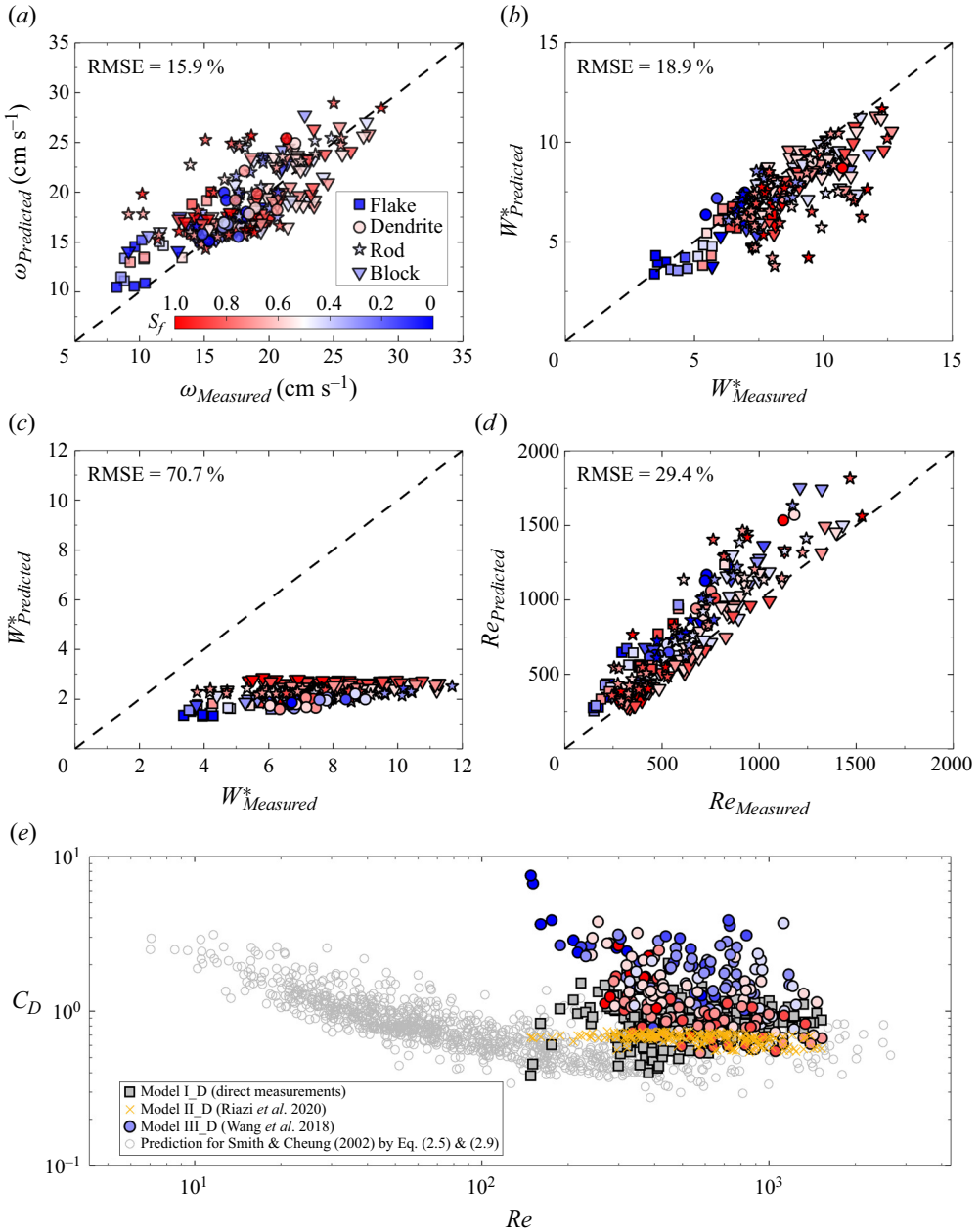


Figure 15. Comparison between the measured and predicted settling velocity in (a–d) and drag coefficient in (e). There is a large difference in the prediction accuracy among different velocity and drag models. (a) Model I_V (Riazi *et al.* 2020). (b) Model II_V (Dietrich 1982). (c) Model III_V (Li *et al.* 2020). (d) Model IV_V (Alcerreca *et al.* 2013). (e) C_D versus Re .

constant $P = 3$, with RMSE = 18.9 % (figure 15b). Similar to model I_V, this model II_V predicts the velocity of rod grains less well.

Model III_V of Li *et al.* (2020) increasingly underpredicts ω with increasing ω (figure 15b). This model gives good prediction of ω for very low $S_f < 0.2$ and the flake grains, but highly underestimates ω for high S_f (figure 15b). The overall performance of

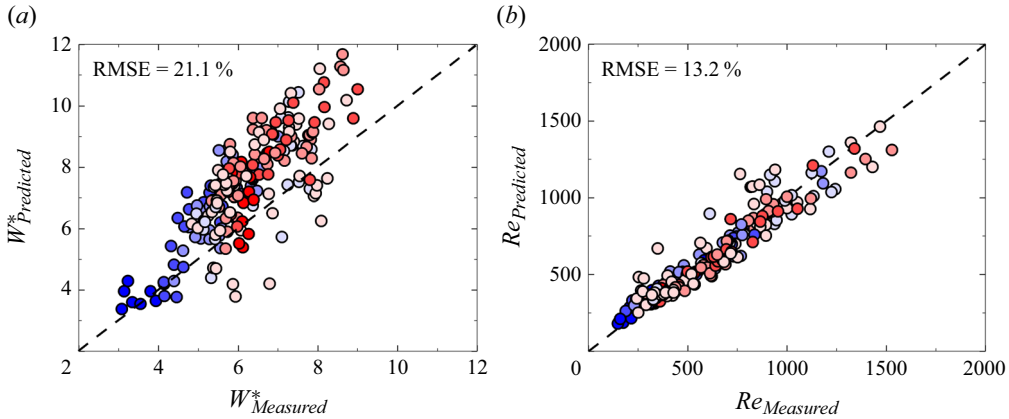


Figure 16. Comparison between the measured and predicted settling velocity by (a) the new model (3.2), and (b) the new model (3.4). The new models perform better than the original models in figures 15(c,d).

this model (RMSE = 70.7 %) is less good than for models I_V and II_V. This is expected given that this model was developed for platy grains in Li *et al.* (2020). Finally, model IV_V of Alcerreca *et al.* (2013) also shows good performance in predicting Re in which ω is embedded, with RMSE = 29.4 % (figure 15d). Specifically, this model predicts Re very well when $S_f \gtrsim 0.5$, but overpredicts ω for $S_f \lesssim 0.5$.

Figure 15(e) presents a comparison between different models for estimating drag coefficients, combined with predictions of Smith & Cheung (2002) by using (2.5) and (2.9). The results of model I_D (direct measurements) agree well with the predictions for Smith & Cheung (2002) using (2.5) and (2.9). Model II_D of Riazi *et al.* (2020) provides a nearly constant predicted value 0.7, which is below the mean value (0.89) of model I_D. The results of model III_D of Wang *et al.* (2018) are in good agreement with those of model I_D for high $S_f \gtrsim 0.5$, but are higher than measured C_D for low $S_f \lesssim 0.5$.

Figure 14 shows the dependence of the model performance on S_f and D^* . This informs us how to improve the predicting accuracy of these models. For instance, we have demonstrated in figure 14(a) the increasing trend of W^* with S_f and D^* . These two variables are already incorporated into model III_V in (2.14). However, figure 15(c) shows that model III_V of Li *et al.* (2020) increasingly underpredicts W^* with the increase of W^* . This suggests that the empirical coefficient associated with S_f and D^* in the model needs to be modified to better reflect the dependence of W^* on S_f and D^* . Following this, we refine the empirical coefficients a , b and c in (2.14a) by using least squares regression based on our experimental data, which gives a newly modified model as

$$W^* = 10^{0.47 \log D^* + 0.47 \log S_f + 0.083}. \quad (3.2)$$

Figure 16(a) shows that the performance of the newly modified model (3.2) is significantly improved with RMSE = 21.1 %, which is much lower than RMSE = 70.7 % for model III_V of Li *et al.* (2020).

Similarly, as the performance of model IV_V of Alcerreca *et al.* (2013) is strongly dependent on the value of S_f (see figure 15d), incorporating S_f into model IV_V will improve the model performance. Following this, we propose here a new form of velocity model as

$$Re = (S_f)^{(a)} \left(\sqrt{22 + bD^{*2}} - c \right)^{3/2}. \quad (3.3)$$

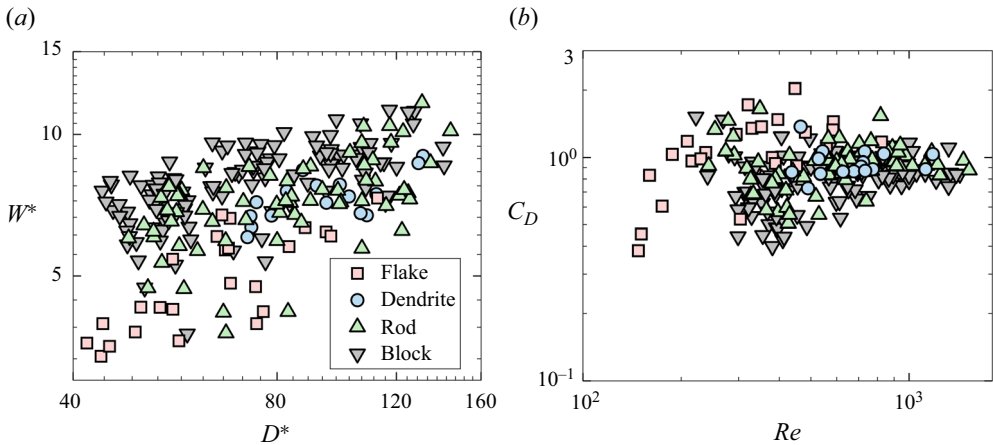


Figure 17. (a) The variation of settling velocity with the dimensionless diameter. (b) The variation of drag coefficient with the Reynolds number. Types of grains, classified based on the method of Wang *et al.* (2019), are differentiated by different symbols.

This form is similar to model IV_V of Alcerreca *et al.* (2013) but with a newly added term $(S_f)^a$. The unknown parameters a , b and c in this extended model can be determined by using least squares regression, which gives the new model as

$$Re = (S_f)^{0.147} \left(\sqrt{22 + 0.932D^{*2}} + 4.804 \right)^{3/2}. \quad (3.4)$$

It is seen that the performance of this model (3.4) is significantly improved (figure 16b). The value of RMSE is down to 13.2 %, which is much lower than the value for model IV_V (figure 15d).

In summary, it is more convenient to adopt the drag model II_D as it requires only the input of the nominal diameter of a particle and the kinematic viscosity of fluid. In contrast, model III_D needs to run an iterative solution between multiple equations in (2.7). Model II_D also outperforms model III_D (figure 15e). Regarding prediction of settling velocity, it is recommended to use our extended model (3.4) due to its simplicity of calculation and the highest accuracy (RMSE = 13.2 %; see figure 16b).

4. Discussion

4.1. Dependence of settling velocity on the grain type

In § 3.1, we demonstrated the dependence of descent regimes on the grain type. One may hypothesise that the settling velocity should also have dependency on the grain type. To check this hypothesis, we have mapped our experimental data of settling velocity and drag coefficient into the W^*-D^* and $Re-C_D$ parameter spaces, respectively, in figures 17(a,b). Whilst the flake grains generally have lowest velocity, the block grains generally have the highest velocity (see figure 17a). On the contrary, the block grains generally have the smallest drag coefficient, and the flake grains generally have the largest drag coefficient (figure 17b). The data points of the flake grains are separated from the main body of data points (see figure 17b). Therefore, figure 17 demonstrates the dependency of settling velocity and drag coefficient on the grain type.

Coefficient	All data	Block	Dendrite	Flake	Rod
a	0.47	0.479	0.286	0.532	0.369
b	0.47	0.532	0.314	0.464	0.015
c	0.083	0.071	0.421	−0.058	0.155
RMSE	21.1 %	19.4 %	5.9 %	11.20 %	16.6 %

Table 5. Modified models (in the form of (2.14)) for each type of grain for predicting the dimensionless settling velocity W^* .

This demonstrated dependency informs us in developing a specified model for each type of grain. These models take the form of (2.14). The coefficients of a , b and c are again determined by least squares regression based on our experimental data, as detailed in table 5. It is seen that the specified models for each type of grain have different levels of predictive performance. In comparison to the model of Li *et al.* (2020), the modified model for dendrite grains has achieved much better performance with only RMSE = 5.9 % (see table 5). The significantly improved performance for the dendrite grains suggests that to have better predictability, it is possible to categorise the coral grains first and then develop a model for each type of grain.

5. Conclusions

In this paper, a series of laboratory experiments was conducted to investigate the settling motion of 222 coral grains. The geometry of these grains was measured by the image recognition technique, the grain density was measured with the drainage method, and the settling trajectory was reconstructed through particle-filtering-based object tracking.

Three descent regimes of settling motions, namely, fluttering, chaotic and tumbling, were classified based on the reconstructed three-dimensional trajectory, the variation of spiral radius with time, and the velocity spectra. The fluttering regime is characterised by a three-dimensional spiral trajectory; in the tumbling regime, the particle drifts sideways when it settles downwards. This regime includes two sub-regimes, i.e. the steady drifting regime where the particle purely drifts, and the oscillatory drifting regime in which small-scale oscillations are superimposed on the drifting process. The chaotic regime is characterised by a random combination of drifting and spiral motions.

By using existing classification methods, the 222 coral grains were categorised into different types of grains. We have presented the probability of occurrence of each regime for each type of grain. Based on the 222 data sets, we have demonstrated that if one randomly picks up one coral grain, then the probabilities of occurrence of the tumbling, chaotic and fluttering regimes are approximately 26 %, 42 % and 32 %, respectively.

We then show that, first, the dimensionless settling velocity generally increases with the non-dimensional diameter D^* and Corey shape factor S_f , and second, the drag coefficient generally decreases with the Reynolds number Re and S_f . The demonstrated dependencies of W^* and C_D provide a physical basis for applying existing empirical models of settling velocity and drag coefficient to coral grains considered herein. The applicability of a range of models of settling velocity and drag coefficient is then validated against the 222 coral grains. It is found that the performance of these models depends on the grain geometry. For instance, the velocity model of Alcerreca *et al.* (2013) and the drag model of Wang *et al.* (2018) perform less well for the grains with low values of S_f .

We have made improvements in the predictive capacity of settling velocity. First, we have extended the models of Li *et al.* (2020) and Alcerreca *et al.* (2013), which gives two new models with much better performance. Second, we modified the model of Li *et al.* (2020) for each type of grain, including, block, dendrite, flake and rod. This provides an idea of how to improve the predictive capacity of settling velocity through pre-categorising the grains.

In a future study, the objective could be replacing the first order shape descriptors (e.g. Corey shape factor) with the second or third order shape descriptors in the settling velocity models. In experiments, it may be possible to take macro-photographs of coral particles to obtain information about the rotation movement of the coral particles during settlement. However, the filming range has to be reduced because of the limited range of pixels of the camera. Using multiple cameras simultaneously may solve this problem.

Supplementary material. Supplementary material is available at <https://doi.org/10.1017/jfm.2024.469>.


Acknowledgements. The authors really appreciate insightful and constructive comments from five anonymous reviewers, which have helped to improve the quality of this paper significantly.

Funding. This study was financially supported by the National Key Research and Development Program of China (grant no. 2021YFB2601100), the National Natural Science Foundation of China (grant no. 52271257) and the Natural Science Foundation of Hunan Province (grant no. 2022JJ10047).

Declaration of interests. The authors report no conflict of interest.

Data availability statement. The data for experimental results (i.e. shape characteristics, settling velocity and classification results of coral grains) of this study are openly available at <https://datadryad.org/stash/share/atsTCBGvDIMEirFyfMgmaQxceYnKly5HfilXv9P4Src>.

Author ORCIDs.

-  Jie Chen <https://orcid.org/0000-0002-9930-0323>;
-  Zhen Yao <https://orcid.org/0000-0003-0920-1602>;
-  Fei He <https://orcid.org/0000-0001-7364-5641>.

Appendix. Definition sketches

A	Area of image
$A_{eq, sph}$	Surface area of volume-equivalent sphere
A_{ell}	Surface area of irregular particles
A_s	Surface area of particle
A_P	Projected area
C_A	Area of minimum convex hull
C_D	Drag coefficient
$C_{D, sph}$	Drag coefficient of spherical particle
C_P	Perimeter of minimum convex hull
D_A	Diameter of circle with same area as projection area of particle
D_{disk}	Diameter of disk
D_P	Diameter of circle with same perimeter as image
D_l	Longest orthogonal dimension of particle
D_m	Intermediate orthogonal dimension of particle
D_s	Shortest orthogonal dimension of particle
D_n	Nominal diameter of particle

The settling motion of coral grains in still water

$D_{eq, sph}$	Diameter of volume-equivalent sphere
D_{sg}	Sphere diameter
D^*	Dimensionless diameter
F_a	Distance between two parallel tangents of particle at arbitrary angle
g	Gravitational acceleration
h	Thickness of disk
I_p	Moment of inertia
I^*	Dimensionless moment of inertia
L	Maximum Feret diameter
P	Roundness of particle
P_i	Perimeter of image
$P_{p, max}$	Perimeter of maximum projection area of particle
P_{eq}	Perimeter of circle of equal maximum projection area
R_0	Roundness
Re	Particle Reynolds number
S	Specific gravity of particle
S_A	Superficial area
S_{CA}	Superficial area of convex hull
S_0	Convexity ratio
S_P	Relative sphericity
S_f	Shape factor of particles
T	Minimum Feret diameter
V	Volume of coral grain
V_P	Particle volume
W	Median Feret diameter
W^*	Dimensionless settling velocity
X	Inverse circularity
ρ	Density of water
ρ_s	Density of coral grain
ω	Particle settling velocity
ν	Kinematic viscosity of ambient water
μ	Dynamic viscosity of water
χ	Aspect ratio
Ψ	Ratio of sphericity

REFERENCES

- ALCERRECA, J.C., SILVA, R. & MENDOZA, E. 2013 Simple settling velocity formula for calcareous sand. *J. Hydraul. Res.* **51** (2), 215–219.
- ALLDREDGE, A.L. & GOTSCHALK, C. 1988 In situ settling behavior of marine snow. *Limnol. Oceanogr.* **33** (3), 339–351.
- ALMEDEIJ, J. 2008 Drag coefficient of flow around a sphere: matching asymptotically the wide trend. *Powder Technol.* **186** (3), 218–223.
- BABCOCK, R. & SMITH, L. 2002 Effects of sedimentation on coral settlement and survivorship. In *Proceedings of the Ninth International Coral Reef Symposium, Bali, 23–27 October 2000*, vol. 1, pp. 245–248. Citeseer.
- BARRETT, P.J. 1980 The shape of rock particles, a critical review. *Sedimentology* **27** (3), 291–303.
- BLOTT, S.J. & PYE, K. 2008 Particle shape: a review and new methods of characterization and classification. *Sedimentology* **55** (1), 31–63.

- CHEN, J., YAO, Z., JIANG, C., WU, Z., DENG, B., LONG, Y. & BIAN, C. 2022 Experiment study of the evolution of coral sand particle clouds in water. *China Ocean Engng* **36** (5), 720–733.
- COREY, A.T., ALBERTSON, M.L., FULTS, J.L., ROLLINS, R.L., GARDNER, R.A., KLINGER, B. & BOCK, R.O. 1949 Influence of shape on the fall velocity of sand grains. PhD thesis, Colorado A & M College.
- DIETRICH, W.E. 1982 Settling velocity of natural particles. *Water Resour. Res.* **18** (6), 1615–1626.
- DONG, X., *et al.* 2023 Metagenomic views of microbial communities in sand sediments associated with coral reefs. *Microbiol. Ecol.* **85** (2), 465–477.
- DUAN, Z., HE, B. & DUAN, Y. 2015 Sphere drag and heat transfer. *Sci. Rep.* **5** (1), 12304.
- FIELD, S.B., KLAUS, M., MOORE, M.G. & NORI, F. 1997 Chaotic dynamics of falling disks. *Nature* **388** (6639), 252–254.
- GRIFFITHS, J.C. 1967 Scientific method in analysis of sediments. *Technometrics* **11** (2), 406.
- HEILBRONNER, R. & BARRETT, S. 2013 *Image Analysis in Earth Sciences: Microstructures and Textures of Earth Materials*. Springer Science & Business Media.
- HEISINGER, L., NEWTON, P. & KANSO, E. 2014 Coins falling in water. *J. Fluid Mech.* **742**, 243–253.
- HENTSCHEL, M.L. & PAGE, N.W. 2003 Selection of descriptors for particle shape characterization. *Part. Part. Syst. Char.* **20** (1), 25–38.
- HONGBING, Y.U., SUN, Z. & CHENG, T. 2006 Physical and mechanical properties of coral sand in the Nansha Islands. *Mar. Sci. Bull.* **8** (2), 31–39.
- ILLENBERGER, W.K. 1991 Pebble shape (and size!). *J. Sedim. Res.* **61** (5), 756–767.
- JONES, R., BESSELL-BROWNE, P., FISHER, R., KLONOWSKI, W. & SLIVKOFF, M. 2016 Assessing the impacts of sediments from dredging on corals. *Mar. Pollut. Bull.* **102** (1), 9–29.
- KHATMULLINA, L. & ISACHENKO, I. 2017 Settling velocity of microplastic particles of regular shapes. *Mar. Pollut. Bull.* **114** (2), 871–880.
- DE KRUIJF, M., SLOOTMAN, A., DE BOER, R.A. & REIJMER, J.J.G. 2021 On the settling of marine carbonate grains: review and challenges. *Earth-Sci. Rev.* **217**, 103532.
- KRUMBEIN, W.C. 1941 Measurement and geological significance of shape and roundness of sedimentary particles. *J. Sedim. Res.* **11** (2), 64–72.
- KWAN, A.K.H., MORA, C.F. & CHAN, H.C. 1999 Particle shape analysis of coarse aggregate using digital image processing. *Cement Concrete Res.* **29** (9), 1403–1410.
- LI, Y., YU, Q., GAO, S. & FLEMMING, B.W. 2020 Settling velocity and drag coefficient of platy shell fragments. *Sedimentology* **67** (4), 2095–2110.
- LÜTTIG, G. 1956 Eine neue, einfache gerölmorphometrische methode. *E&G Quart. Sci. J.* **7** (1), 13–20.
- MAIKLEM, W.R. 1968 Some hydraulic properties of bioclastic carbonate grains. *Sedimentology* **10** (2), 101–109.
- MORA, C.F. & KWAN, A.K.H. 2000 Sphericity, shape factor, and convexity measurement of coarse aggregate for concrete using digital image processing. *Cement Concrete Res.* **30** (3), 351–358.
- Oakey, R.J., GREEN, M., CARLING, P.A., LEE, M.W.E., SEAR, D.A. & Warburton, J. 2005 Grain-shape analysis – a new method for determining representative particle shapes for populations of natural grains. *J. Sedim. Res.* **75** (6), 1065–1073.
- PRATCHETT, M.S. 2005 Dynamics of an outbreak population of *Acanthaster planci* at Lizard Island, northern Great Barrier Reef (1995–1999). *Coral Reefs* **24** (3), 453–462.
- RAAGHAV, S.K.R., POELMA, C. & BREUGEM, W.-P. 2022 Path instabilities of a freely rising or falling sphere. *Int. J. Multiphase Flow* **153**, 104111.
- RIAZI, A. & TÜRKER, U. 2018 A genetic algorithm-based search space splitting pattern and its application in hydraulic and coastal engineering problems. *Neural Comput. Applics.* **30**, 3603–3612.
- RIAZI, A. & TÜRKER, U. 2019 The drag coefficient and settling velocity of natural sediment particles. *Comput. Part. Mech.* **6** (3), 427–437.
- RIAZI, A., VILA-CONCEJO, A., SALLES, T. & TÜRKER, U. 2020 Improved drag coefficient and settling velocity for carbonate sands. *Sci. Rep.* **10** (1), 9465.
- ROGERS, C.S. & RAMOS-SCHARRÓN, C.E. 2022 Assessing effects of sediment delivery to coral reefs: a Caribbean watershed perspective. *Front. Mar. Sci.* **8**, 2129.
- ROUSE, H., *et al.* 1938 *Fluid Mechanics for Hydraulic Engineers*, vol. 1. McGraw-Hill.
- SCALES, H., BALMFORD, A. & MANICA, A. 2007 Impacts of the live reef fish trade on populations of coral reef fish off northern Borneo. *Proc. R. Soc. Lond. B* **274** (1612), 989–994.
- SCHULZ, E.F., WILDE, R.H. & ALBERTSON, M.L. 1954 Influence of shape on the fall velocity of sedimentary particles. PhD thesis, Colorado State University.

The settling motion of coral grains in still water

- SLOOTMAN, A., DE KRUIJF, M., GLATZ, G., EGGENHUISEN, J.T., ZÜHLKE, R. & REIJMER, J.J.G. 2023 Shape-dependent settling velocity of skeletal carbonate grains: implications for calciturbidites. *Sedimentology* **70** (6), 1683–1722.
- SMITH, D.A. & CHEUNG, K.F. 2002 Empirical relationships for grain size parameters of calcareous sand on Oahu, Hawaii. *J. Coast. Res.* **18** (1), 82–93.
- SNEED, E.D. & FOLK, R.L. 1958 Pebbles in the lower Colorado River, Texas: a study in particle morphogenesis. *J. Geol.* **66** (2), 114–150.
- WADELL, H. 1932 Volume, shape, and roundness of rock particles. *J. Geol.* **40** (5), 443–451.
- WADELL, H. 1933 Sphericity and roundness of rock particles. *J. Geol.* **41** (3), 310–331.
- WANG, B., MENG, Q., WEI, C., CHEN, M., YAN, K. & ZHANG, P. 2019 Quantitative experimental study of the morphology of coral sand and gravel particles under multiple projection surfaces. *Rock Soil Mech.* **40** (10), 3871–3878.
- WANG, X., WU, Y., CUI, J., ZHU, C.-Q. & WANG, X.-Z. 2020 Shape characteristics of coral sand from the South China Sea. *J. Mar. Sci. Engng* **8** (10), 803.
- WANG, Y., ZHOU, L., WU, Y. & YANG, Q. 2018 New simple correlation formula for the drag coefficient of calcareous sand particles of highly irregular shape. *Powder Technol.* **326**, 379–392.
- ZINGG, T. 1935 Beitrag zur schotteranalyse. PhD thesis, ETH Zurich.